

## Clinical study of $^{99m}\text{Tc}$ -3P-RGD2 peptide imaging in osteolytic bone metastasis

Guoqiang Shao<sup>1</sup>, Wei Gu<sup>2</sup>, Muhong Guo<sup>1</sup>, Shiming Zang<sup>1</sup>, Jinjing Fu<sup>1</sup>, Shuang Liu<sup>3</sup>, Feng Wang<sup>1</sup> and Zizheng Wang<sup>1</sup>

<sup>1</sup> Department of Nuclear Medicine, Nanjing First Hospital, Nanjing Medical University, Nanjing, China

<sup>2</sup> Department of Respiration, Nanjing First Hospital, Nanjing Medical University, Nanjing, China

<sup>3</sup> School of Health Sciences, Purdue University, West Lafayette, IN, USA

Correspondence to: Zizheng Wang, email: 13770920210@163.com

Feng Wang, email: 1377950188@qq.com

**Keywords:** osteolytic metastasis; targeted imaging; integrin  $\alpha_v\beta_3$ ; RGD peptide; lung cancer

**Received:** January 06, 2017

**Accepted:** April 04, 2017

**Published:** April 27, 2017

Copyright: Shao et al. This is an open-access article distributed under the terms of the Creative Commons Attribution License 3.0 (CC-BY 3.0), which permits unrestricted use, distribution, and reproduction in any medium, provided the original author and source are credited.

### ABSTRACT

**Objective:** To investigate the value of integrin  $\alpha_v\beta_3$  targeted imaging with  $^{99m}\text{Tc}$ -HYNIC-PEG<sub>4</sub>-E[PEG<sub>4</sub>-c(RGDfk)]<sub>2</sub> ( $^{99m}\text{Tc}$ -3P-RGD<sub>2</sub>) as a radiotracer in detecting osteolytic bone metastases.

**Methods:** This is a retrospective study involving a cohort of 69 consecutive patients including 59 with lung cancer and 10 with other cancers. Patients were required to receive whole body scan (WBS) and regional SPECT/CT imaging with  $^{99m}\text{Tc}$ -3P-RGD<sub>2</sub> (RGD imaging) and  $^{99m}\text{Tc}$ -MDP (MDP imaging) as a radiotracer successively within days. Final diagnosis was based on comprehensive assessment of all available data including case history, CT, MRI, SPECT/CT, PET/CT, histopathology and 6-12 months follow-up. Visual observation and semiquantitative analysis (T/N: tracer uptake ratio of osteolytic metastases to normal bone) of  $^{99m}\text{Tc}$ -3P-RGD<sub>2</sub> or  $^{99m}\text{Tc}$ -MDP imaging were performed and their detective values for osteolytic metastases were compared.

**Results:** A total of 131 osteolytic metastatic lesions were retrospectively studied. Osteolytic metastases mainly presented as "hot region", occasionally as "cool or normal region" on RGD imaging. The detection sensitivity of RGD WBS for osteolytic metastases was significantly higher than that of  $^{99m}\text{Tc}$ -MDP WBS (80.9% vs. 46.6%,  $p < 0.01$ ). The sensitivity increased to 96.2% (126/131) when combining with SPECT/CT.  $^{99m}\text{Tc}$ -3P-RGD<sub>2</sub> imaging also promoted the detection of unknown primary tumor, lymph node metastases and offered information for clinical staging. T/N of  $^{99m}\text{Tc}$ -3P-RGD<sub>2</sub> in lung adenocarcinoma osteolytic metastases showed no statistical difference compared with that in squamous-cell carcinoma ( $6.84 \pm 3.46$  vs.  $7.33 \pm 3.22$ ,  $t = 0.39$ ,  $p = 0.71$ ). Whereas, it was higher in osteolytic metastases from lung cancer than that from thyroid cancer ( $7.05 \pm 3.01$  vs.  $4.11 \pm 2.67$ ,  $p = 0.03$ ). **Conclusion:**  $^{99m}\text{Tc}$ -3P-RGD<sub>2</sub> peptide imaging showed great potential for detection of osteolytic bone metastasis due to high expression level of integrin  $\alpha_v\beta_3$  on osteoclast and most tumor cells.

### INTRODUCTION

Skeleton is one of the most common sites for metastasis. A majority of patients may present osteolytic

and osteoblastic metastasis, which will result in marked disturbances of bone remodeling that can be lytic and/or blastic. Osteolytic metastasis, a common complication in breast cancer, lung cancer, prostate cancer, or multiple

myeloma [1, 2], brings about significant morbidity of intractable pain, spinal cord compression, pathologic fracture, functional impairment and hypercalcemia [3, 4]. In addition, bone micro-metastasis can serve as an independent predictor of poor outcome in patients with tumor even among lymph node-negative patients with primary tumors of less than 2 cm [5]. Early diagnosis of osteolytic metastasis is definitely important for its correct treatment and better prognosis.

Anatomical imaging (e.g. CT and MRI) has been commonly used for the diagnosis of osteolytic lesions. However, the diagnostic sensitivity of CT is relatively low in cases of a mineral content loss of less than 50% at the lesions sites [6]. Meanwhile, MRI could not readily display bone degradation [7].  $^{99m}\text{Tc}$ -diphosphonates ( $^{99m}\text{Tc}$ -MDP)-based planar bone scan is considered as the standard technique for the detection of skeletal metastasis as it shows high sensitivity, especially for bone lesions with osteogenesis. As is known to all, the accumulation of  $^{99m}\text{Tc}$ -MDP in the bone is highly relied on the osteoblast activity [8]. Absence of  $^{99m}\text{Tc}$ -MDP or high false negative was reported at early period in osteolytic lesions rich in osteoclast, tumor cells and different degree of osteolysis. Therefore, the detection value of  $^{99m}\text{Tc}$ -MDP imaging in osteolytic lesions was lower than that in the osteoblastic lesions [9]. On this basis, it is urgent to develop appropriate imaging technique(s) for the detection of osteoclasts and adjacent tumor cells in patients with osteolytic metastases in an early and accurate manner.

Malignant interaction between tumor cells and osteoclasts in bone microenvironment plays a pivotal role in the pathogenesis of metastatic bone disease such as osteolytic and/or osteoblastic bone metastases. Tumor cells contributed to the recruitment and activation of osteoclasts, which triggered regional osteolysis and tumor cell proliferation [10]. Tumor cells and osteoclasts are the main component of osteolytic metastatic lesions. Integrin  $\alpha_v\beta_3$ , highly expressed in several tumor cells and activated endothelial cells in newly-generated vessels, has been considered as a target for tumor imaging with radiolabeled arginine-glycine-aspartic acid (RGD) peptides and analogues. Furthermore, osteoclast expressing high level of integrin  $\alpha_v\beta_3$  had attracted great attention for positive imaging of osteolytic bone metastasis [11].

$^{99m}\text{Tc}$ -HYNIC-3PEG4-E[c(RGDfK)]<sub>2</sub> ( $^{99m}\text{Tc}$ -3P-RGD<sub>2</sub>) is a cyclic RGD dimmer peptide with high specificity and affinity to integrin  $\alpha_v\beta_3$ . To date,  $^{99m}\text{Tc}$ -3P4-RGD<sub>2</sub> scintigraphy has been commonly used for differential diagnosis of solitary pulmonary nodule, lymph node metastasis and treatment response monitoring [12-15]. This retrospective study was designed to investigate the detective and diagnostic value of  $^{99m}\text{Tc}$ -3P4-RGD<sub>2</sub> imaging for osteolytic bone metastasis.

## MATERIALS AND METHODS

### Patients

This study was approved by the Institute Review Boards of both Nanjing Medical University and Nanjing First Hospital. Written informed consent was obtained from each patient. All reported investigations were conducted in accordance with the Declaration of Helsinki and with our national regulations. Eighty-eight patients were diagnosed with malignant tumors such as primary lung cancer, lung metastases from thyroid cancer, malignant chromaffin-cell tumor, gastric cancer, breast cancer based on the assessment of case history, CT, MRI, SPECT/CT, PET/CT histopathology and 6-12 month follow-up data. Sixty-nine (48.6%) patients presenting pulmonary nodule were suspected with lung cancer and concurrent osteolytic bone metastases. The exclusion criteria were as follows: (i) received treatment before imaging; (ii) pregnant and breastfeeding patients; (iii) those with a history of bone trauma, fracture, and bone inflammation such as tuberculosis within one year; or (iv) those could not accomplish the required examinations because of severe pain or claustrophobia.

### Radiopharmaceutical preparation

$^{99m}\text{Tc}$ -3P-RGD<sub>2</sub> was prepared according to our previous description [16, 17]. Briefly, 1 mL Na $^{99m}\text{Tc}$ O<sub>4</sub> solution (1, 110-1, 850 MBq) was added into lyophilized kit formulation containing 20 mg hydrazinonicotinamide-PEG4-E[PEG4-c(RGDfK)]<sub>2</sub> (HYNIC-3P-RGD<sub>2</sub>), 6.5 mg tricine, 5 mg trisodium triphenylphosphine-3, 39, 399-trisulfonate (TPPTS), 38.5 mg disodium succinate hexahydrate, 40 mg mannitol, and 12.7 mg succinic acid. The reaction system was incubated in water at 100°C for 20 min. The radiochemical purity of the product was > 98% by radio-HPLC. Radiopharmaceuticals were then subject to a 0.20mm Millex-LG filter and diluted to 740MBq/ml for clinical study.

### Imaging protocol

We evaluated all of the patients using  $^{99m}\text{Tc}$ -3P-RGD<sub>2</sub> imaging and  $^{99m}\text{Tc}$ -MDP imaging [including both whole body scan (WBS) and SPECT-CT with consistent imaging field] within one week. The imaging was performed on a SPECT-CT equipment (Symbia T6, Simense, Germany) according to manufacturer's instructions. All patients had urinated completely prior to imaging. Imaging was performed within one week. Anterior and posterior WBS was performed 1h after intravenous injection of  $^{99m}\text{Tc}$ -3P-RGD<sub>2</sub> (750±37.5MBq,

in 1.0 ml saline) or 3h after intravenous injection of  $^{99m}\text{Tc}$ -MDP ( $750\pm 75\text{MBq}$ , in 1.0 ml saline). WBS imaging parameters included low-energy high-resolution collimators, bed movement speed of 10.0 cm/min, energy window of 20% width and centered on 140keV. SPECT data set was obtained (ZOOM of 1.3, 256 by 256 matrix size, 30s/Frame for 32 frames and  $180^\circ$  each head of the dual head-camera) immediately after WBS using a low-energy high-resolution collimator at 140 keV with a window width of 20%. Then the data were reconstructed with ordered subset expectation maximization (OSEM). CT scan was performed in the same anatomic locations as SPECT with a tube voltage of 130 kV and current intensity at 120 mA/slice with a slice thickness of 3 mm.

## Image analysis

Image analysis was performed by 2 nuclear medicine physicians and 2 radiologists blinded to the case history, examination results, and pathologic diagnosis or follow up data. Visual observation and semiquantitative analysis of  $^{99m}\text{Tc}$ -3P-RGD<sub>2</sub> or  $^{99m}\text{Tc}$ -MDP imaging were performed based on the accumulation of radiotracer at the lesion sites comparing to the contralateral or surrounding normal bone tissues (T/N ratio). The 4-point grade system was also adopted to describe the uptake degree of radiotracers in osteolytic lesions [18]: grade 0, tracer uptake similar to surrounding normal bone structure; grade 1, uptake less ( $^{99m}\text{Tc}$ -MDP) or slightly higher ( $^{99m}\text{Tc}$ -3P-RGD<sub>2</sub>) than surrounding normal bone structure; grade 2, uptake significantly less ( $^{99m}\text{Tc}$ -MDP) or higher ( $^{99m}\text{Tc}$ -3P-RGD<sub>2</sub>) than surrounding normal bone structure; grade 3, abnormal aggregation of  $^{99m}\text{Tc}$ -3P-RGD<sub>2</sub> or almost absence of  $^{99m}\text{Tc}$ -MDP with or without regional accumulation surrounding the lesion or regional aggregation of  $^{99m}\text{Tc}$ -MDP in confirmed osteolytic lesions. Osteolytic bone metastasis was ascertained according to any of the following criteria: tracer uptake score greater or equal to grade 2 on either  $^{99m}\text{Tc}$ -3P-RGD<sub>2</sub> or  $^{99m}\text{Tc}$ -MDP imaging; tracer uptake score equals to grade 1 on both  $^{99m}\text{Tc}$ -3P-RGD<sub>2</sub> and  $^{99m}\text{Tc}$ -MDP imaging especially with bone pain symptom, or increased uptake on  $^{99m}\text{Tc}$ -MDP imaging but confirmed to be osteolytic on other imaging modalities such as CT (including CT on SPECT-CT imaging),  $^{18}\text{F}$ -FDG PET-CT imaging, and MRI.

## Verification of osteolytic bone metastases

The final diagnosis of osteolytic bone metastases was based on histopathology, imaging findings (i.e. CT, SPECT/CT, PET/CT, MRI) and clinical follow-up data using specific standards as follows: (a) histopathologically proven; and (b) Besides primary malignancy diagnosis, CT or magnetic resonance imaging (MRI) results indicated obvious bone destruction without osteogenic

imaging performance. (c) Increased range and/or lesions of bone destruction during follow-up [19-21]. During the clinical follow-up, multiple imagings were required for the patients, and all patients were followed up at least 6 months. Lesions exhibiting both osteolytic and osteosclerotic changes were verified by either type, depending on the predominant changes [22].

## Statistical analysis

Data were expressed as mean  $\pm$  standard deviation. The number of osteolytic bone metastases detected using  $^{99m}\text{Tc}$ -3P-RGD<sub>2</sub> and  $^{99m}\text{Tc}$ -MDP was compared. Sensitivity of  $^{99m}\text{Tc}$ -3P-RGD<sub>2</sub> imaging and  $^{99m}\text{Tc}$ -MDP imaging modality were compared using McNemar test. The lesion detection consistency of the two modalities were compared using the Kappa test.  $P < 0.05$  was considered to be statistically significant.

## RESULTS

### Patient characteristics and distribution of osteolytic lesions

Sixty-nine cases with malignant tumor were confirmed with 131 osteolytic metastases according to the comprehensive data based on case history, CT, MRI, SPECT/CT, PET/CT examinations, histopathology and 6-12 months follow-up. Patients' characteristics and the number of osteolytic, lymph node metastases were listed in Table 1.

### Visual analysis of osteolytic bone metastasis on $^{99m}\text{Tc}$ -MDP and $^{99m}\text{Tc}$ -3P-RGD<sub>2</sub> imaging

The distribution of the 131 osteolytic bone metastases was summarized in Table 2. Among these metastases, 57 were localized in the neck and chest including cervical vertebra (8), thoracic vertebra (11), sternum (7), rib (31), 20 in the lumbar vertebra, 33 in the sacrococcyx and pelvis, and 21 in the appendicular skeleton including limb (14) and shoulder (7).

Based on visual analysis, osteolytic bone metastases were mainly manifested as significant accumulation (hot area, Fig. 1A and 1B), occasionally slight higher uptake (Fig. 1C) or absence of  $^{99m}\text{Tc}$ -3P-RGD<sub>2</sub> on WBS and SPECT-CT imaging with or without bone destruction on CT (cold area, Fig. 1D). For  $^{99m}\text{Tc}$ -MDP, osteolytic bone metastases were manifested as "cold area" and occasionally as increased uptake (Fig. 2 and 3). Single osteolytic metastasis (with a long diameter of 4.1 cm) was manifested as cold region with slight elevation of  $^{99m}\text{Tc}$ -MDP uptake in the peripheral part, while negative

**Table 1: Demographic profile and the final histological diagnosis of 69 patients with malignant tumors and distant metastasis**

Category	number of people	proportion (%)	number of osteolytic metastasis	number of lymph node metastasis
<b>Gender</b>				
Male	39	56.5		
Female	30	43.5		
<b>Tumor type</b>				
Lung cancer				
adenocarcinoma	27	39.1	74	4
Squamous-cell carcinoma	32	46.4	40	15
Thyroid cancer	3	4.3	4	2
Malignant chromaffin-cell tumor	2	2.9	5	
breast cancer	1	1.4	1	0
Gastric cancer	4	5.8	5	1

findings were observed on  $^{99m}\text{Tc}$ -3P-RGD<sub>2</sub> WBS for the single osteolytic metastasis.

When scored visually based on whole body scan, 30.5% (40/131) of osteolytic metastatic lesions was graded equally between  $^{99m}\text{Tc}$ -MDP and  $^{99m}\text{Tc}$ -3P-RGD<sub>2</sub>, 57.3% (75/131) was graded higher on  $^{99m}\text{Tc}$ -3P-RGD<sub>2</sub> and 12.2% (16/131) was graded higher on  $^{99m}\text{Tc}$ -MDP. Comparative analysis of  $^{99m}\text{Tc}$ -3P-RGD<sub>2</sub> and  $^{99m}\text{Tc}$ -MDP whole body scan imaging (WBS) in the detection of osteolytic metastases was summarized in Table 2. The sensitivity of

$^{99m}\text{Tc}$ -3P-RGD<sub>2</sub> WBS on metastatic lesions was superior to that of  $^{99m}\text{Tc}$ -MDP WBS, especially in axial skeleton.

The score grade showed obvious change in both imaging modalities after SPECT-CT (Table 3).  $^{99m}\text{Tc}$ -3P-RGD<sub>2</sub> imaging also displayed abnormal uptake in primary tumor and distant metastatic lesions (Figure 4 and 5, Table 1). Regional accumulation of  $^{99m}\text{Tc}$ -3P-RGD<sub>2</sub> contributed to the detection of primary tumor in thyroid cancer ( $n = 3$ ), breast cancer ( $n = 1$ ), malignant chromaffin-cell tumor ( $n = 2$ ), gastric cancer ( $n = 4$ ), lymph node metastasis (Figure

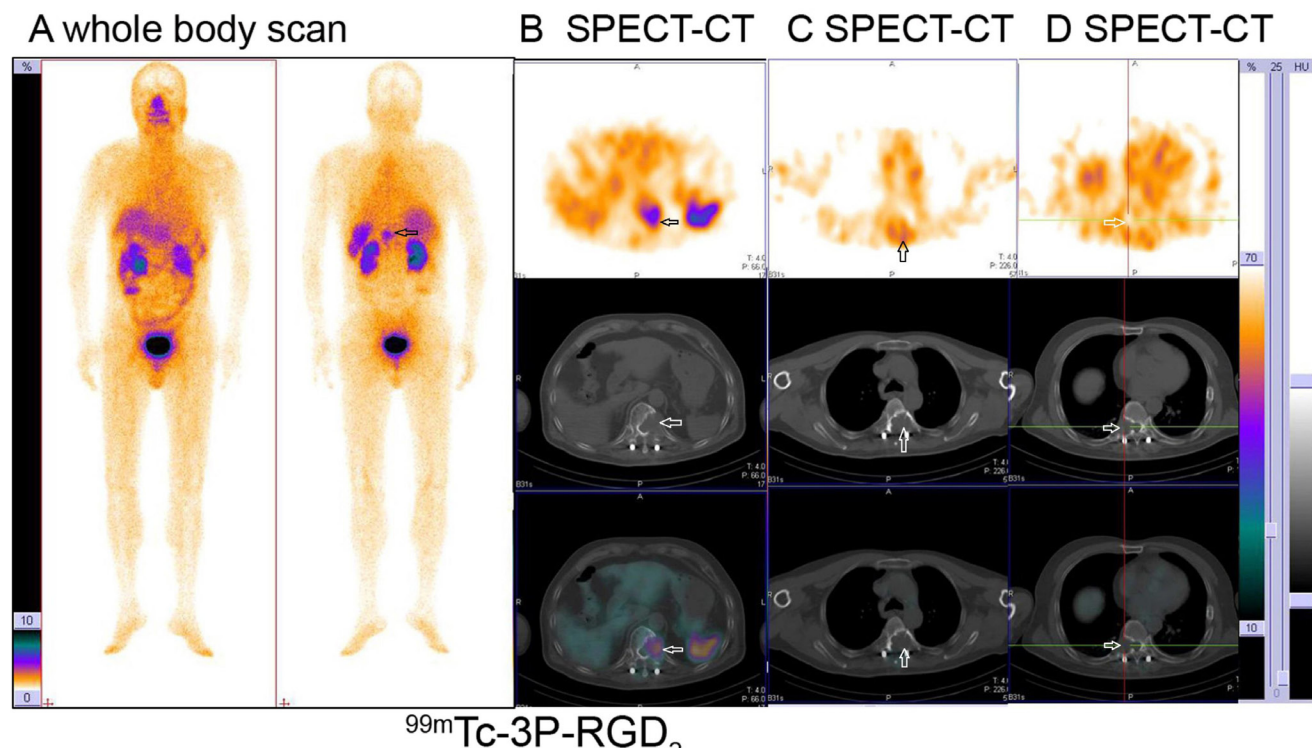


**Figure 1: Osteolytic bone metastases from lung cancer displayed as significant accumulation (hot area) (A, B), slight higher uptake (C) or absence (cold area) (D) of  $^{99m}\text{Tc}$ -3P-RGD<sub>2</sub> on whole body planar scan (A) and SPECT-CT (B, C, D) with bone destruction on CT. (see arrows)**

**Table 2: Comparative analysis of  $^{99m}\text{Tc}$ -3P-RGD<sub>2</sub> and  $^{99m}\text{Tc}$ -MDP whole body scan imaging (WBS) in the detection of osteolytic metastases in axial, appendicular skeleton**

Bone area	number of lesions	WBS		p value
		$^{99m}\text{Tc}$ -MDP	$^{99m}\text{Tc}$ -3P-RGD <sub>2</sub>	
axial skeleton	110	60	92	<0.001
appendicular skeleton	21	17	19	>0.05
total	131	77	111	<0.001

5). On this basis, the clinical stage of the 69 patient was changed.

**Detection value of  $^{99m}\text{Tc}$ -3P-RGD<sub>2</sub> and  $^{99m}\text{Tc}$ -MDP imaging for osteolytic bone metastases**

Semiquantification of tracer uptake in osteolytic bone metastasis was expressed as T/N. A large variance (0.73-13.5) was noticed in the  $^{99m}\text{Tc}$ -3P-RGD<sub>2</sub> in tracer uptake in osteolytic bone metastases. T/N on  $^{99m}\text{Tc}$ -3P-RGD<sub>2</sub> WBS was significantly lower than that on SPECT-CT (4.93±2.20 vs. 6.80±3.19, t = 15.1, p < 0.01). The positive rate of  $^{99m}\text{Tc}$ -3P-RGD<sub>2</sub> WBS showed significant increase compared to  $^{99m}\text{Tc}$ -MDP WBS based on T/N analysis (80.9% vs. 46.6%, p < 0.05, Supplemental Table 1). When combining with SPECT-CT, the detective sensitivity of  $^{99m}\text{Tc}$ -3P-RGD<sub>2</sub> imaging increased to 96.2%

(126/131). The osteolytic metastases demonstrated that lower or similar  $^{99m}\text{Tc}$ -3P-RGD<sub>2</sub> uptake was more commonly seen in large size lesions with existence of predominant bone destruction, internal necrosis or/and surrounding cyclic hyperostosis/osteosclerosis. T/N of  $^{99m}\text{Tc}$ -3P-RGD<sub>2</sub> in osteolytic metastatic lesions in lung adenocarcinoma patients showed no statistical difference from that in squamous-cell carcinoma (6.84±3.46 vs. 7.33±3.22, t = 0.39, p = 0.71). T/N of  $^{99m}\text{Tc}$ -3P-RGD<sub>2</sub> in osteolytic metastases from primary lung cancer was significantly higher than that from thyroid cancer (7.05±3.01 vs. 4.11±2.67, p = 0.03).

**DISCUSSION**

$^{99m}\text{Tc}$ -MDP is widely used to detect metastatic bone lesions via adhering to hydroxyapatite crystal and

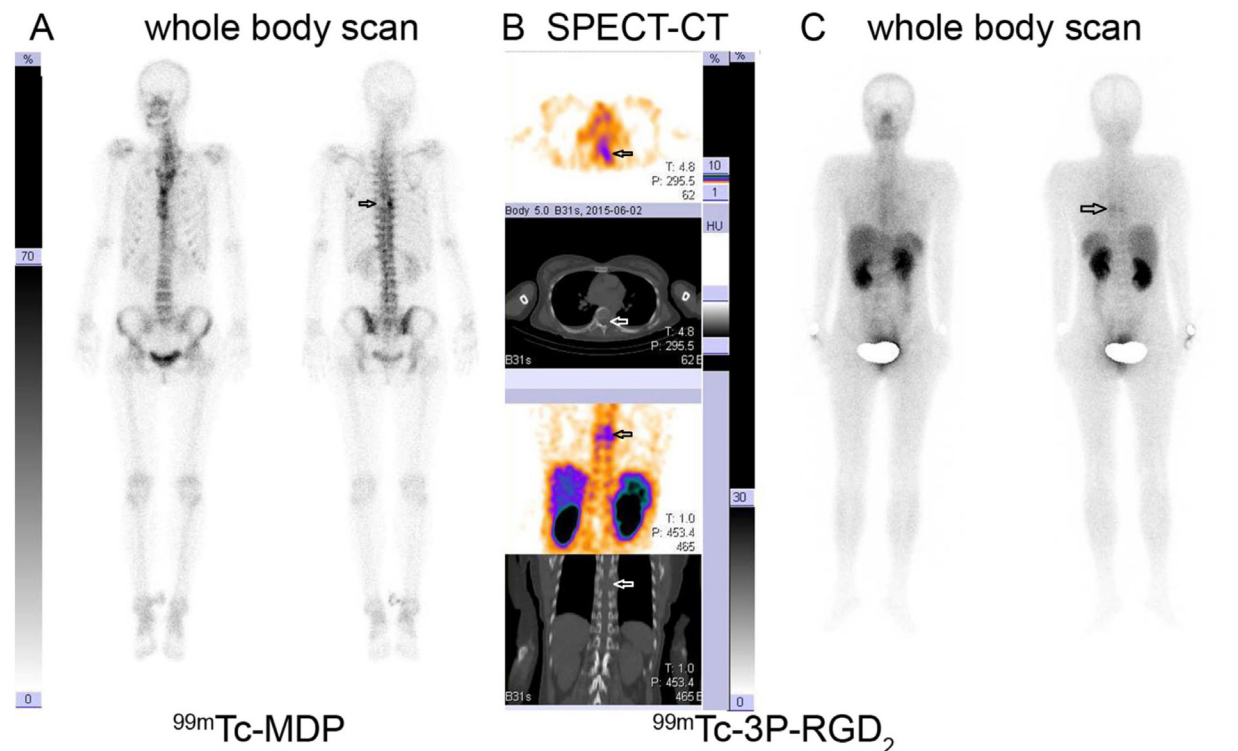


**Figure 2:  $^{99m}\text{Tc}$ -MDP Whole Body Scan (WBS) versus  $^{99m}\text{Tc}$ -3P-RGD<sub>2</sub> WBS and SPECT-CT in a lung cancer patient.**  $^{99m}\text{Tc}$ -MDP WBS demonstrated tracer absence (cold area) in the left side of the 7<sup>th</sup> thoracic vertebral body A.  $^{99m}\text{Tc}$ -3P-RGD<sub>2</sub> SPECT-CT imaging demonstrates bone destruction and corresponding tracer accumulation in the left side of 7<sup>th</sup> thoracic vertebral body and adjacent rib with T/N ratio of 6.31 B.  $^{99m}\text{Tc}$ -3P-RGD<sub>2</sub> WBS displayed as “hot region” in the left side of the 7<sup>th</sup> thoracic vertebral body C. A:  $^{99m}\text{Tc}$ -MDP WBS; B:  $^{99m}\text{Tc}$ -3P-RGD<sub>2</sub> SPECT-CT; C:  $^{99m}\text{Tc}$ -3P-RGD<sub>2</sub> WBS. (see arrows)

**Table 3: Visual analysis of 131 osteolytic bone metastasis on  $^{99m}\text{Tc}$ -3P-RGD<sub>2</sub> and  $^{99m}\text{Tc}$ -MDP WBS imaging and SPECT-CT**

grade	WBS		WBS+SPECT-CT	
	$^{99m}\text{Tc}$ -MDP	$^{99m}\text{Tc}$ -3P-RGD <sub>2</sub>	$^{99m}\text{Tc}$ -MDP	$^{99m}\text{Tc}$ -3P-RGD <sub>2</sub>
0	54	20	27	10
1	15	29	27	32
2	28	54	39	61
3	34	28	38	28

collagen in bone matrix. It is manifested as a “hot zone” in osteoblastic bone metastases even before changes of anatomical structure.  $^{99m}\text{Tc}$ -MDP WBS imaging is superior for the detection of osteoblastic metastases, however, its efficiency in the detection of osteolytic lesions is hampered due to overlapping from normal bone tissues. Osteolytic bone metastasis, characterized by the activation of osteoclasts and the resulting bone resorption, is visualized as a “cold area” (negative imaging) due to absence of  $^{99m}\text{Tc}$ -MDP uptake. However, osteolytic metastatic lesions, consisting of a great number of tumor cells and osteoclasts expressing high level of integrin  $\alpha\nu\beta 3$  and  $\alpha\nu\beta 5$  [23], are visualized as a “hot zone” (positive imaging) as it can bind to  $^{99m}\text{Tc}$ -3P-RGD<sub>2</sub>. This was the main mechanism of  $^{99m}\text{Tc}$ -3P-RGD<sub>2</sub> imaging for the detection of osteolytic bone metastases with high T/N ratio. Our study showed that  $^{99m}\text{Tc}$ -3P-RGD<sub>2</sub> WBS was more effective than  $^{99m}\text{Tc}$ -MDP WBS in the detection of osteolytic bone metastases, which may be related to the following aspects: Firstly, “hot area” was more easy to be visualized than “cold area” on WBS. Secondly, distribution of  $^{99m}\text{Tc}$ -3P-RGD<sub>2</sub>

in normal bone structures was extremely low, which made the osteolytic bone metastases much easier to be detected with low background. Thirdly, overlapping of normal bone structures contributed to low grade for the lesions in vertebra, sternum, sacrococcyx and pelvis, which finally induced misdiagnosis by  $^{99m}\text{Tc}$ -MDP WBS [24].

Clinically, SPECT-CT was performed in presence of abnormality or highly suspicious on WBS images. For the highly suspected patients, it is difficult for a patient to accept the whole body SPECT-CT each time during his first imaging or during regular follow-up. The detection of suspicious osteolytic bone metastases on WBS is of great importance as it serves as a gate for selective SPECT-CT imaging that will facilitate lesion detection, boundary delineation for semiquantitative analysis and accurate diagnosis [25, 26]. The detection value of osteolytic bone metastases increased by about 15% and several patients with score grade increased on both imaging modalities after combining with SPECT-CT. SPECT-CT is vital for  $^{99m}\text{Tc}$ -3P-RGD<sub>2</sub> imaging due to absence of normal skeleton appearance for lesion localization. Furthermore, moderate-

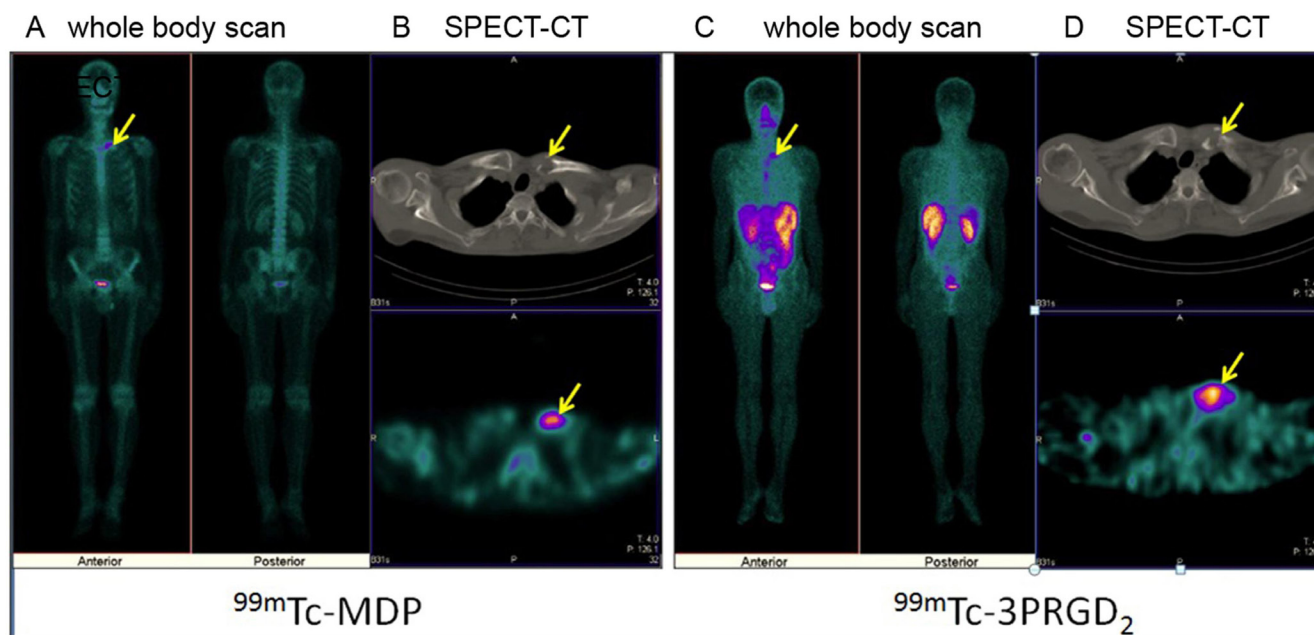


**Figure 3:  $^{99m}\text{Tc}$ -MDP imaging versus  $^{99m}\text{Tc}$ -3P-RGD<sub>2</sub> imaging [Whole Body Scan (WBS) and SPECT-CT] in a patient with lung cancer. Osteolytic bone metastases in the left clavicular head demonstrates as “hot region” on both  $^{99m}\text{Tc}$ -MDP A., B. and  $^{99m}\text{Tc}$ -3P-RGD<sub>2</sub> imaging C., D. and bone destruction on CT(B,D) . A:  $^{99m}\text{Tc}$ -MDP WBS; B:  $^{99m}\text{Tc}$ -MDP SPECT-CT; C:  $^{99m}\text{Tc}$ -3P-RGD<sub>2</sub> WBS; D:  $^{99m}\text{Tc}$ -3P-RGD<sub>2</sub> SPECT-CT. (see arrows).**

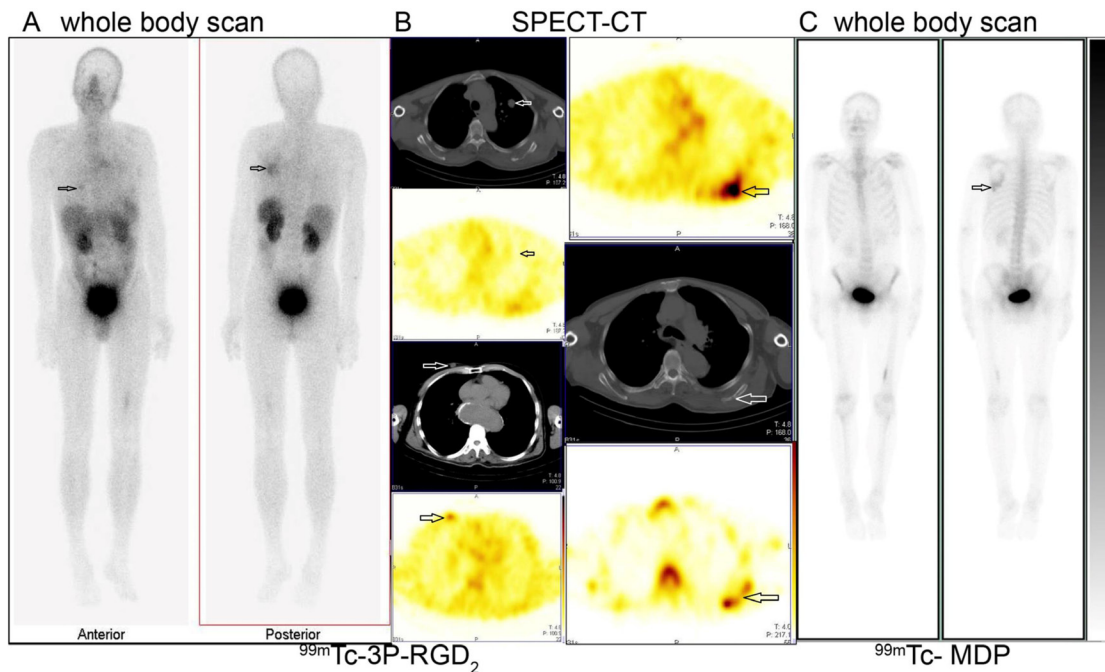


**Figure 4:**  $^{99m}\text{Tc}$ -3P-RGD<sub>2</sub> imaging promoted the detection of primary tumor. High tracer accumulation of  $^{99m}\text{Tc}$ -3P-RGD<sub>2</sub> in right breast (A. left image and B left bottom two images, T/N=3.7) and left scapula (A: right image and B right upper two images) were demonstrated in one breast cancer patient with pulmonary nodule (B. left upper 2 images, T/N=1.08) in the left lung. The osteolytic bone metastasis in the left scapula displayed internal regional absence and slight elevation of  $^{99m}\text{Tc}$ -MDP uptake in the surrounding bone tissues (B: right bottom and C). A:  $^{99m}\text{Tc}$ -3P-RGD<sub>2</sub> whole body scan; B:  $^{99m}\text{Tc}$ -3P-RGD<sub>2</sub> SPECT-CT (the right bottom image is  $^{99m}\text{Tc}$ -MDP SPECT); C.  $^{99m}\text{Tc}$ -MDP whole body scan. (see arrows).

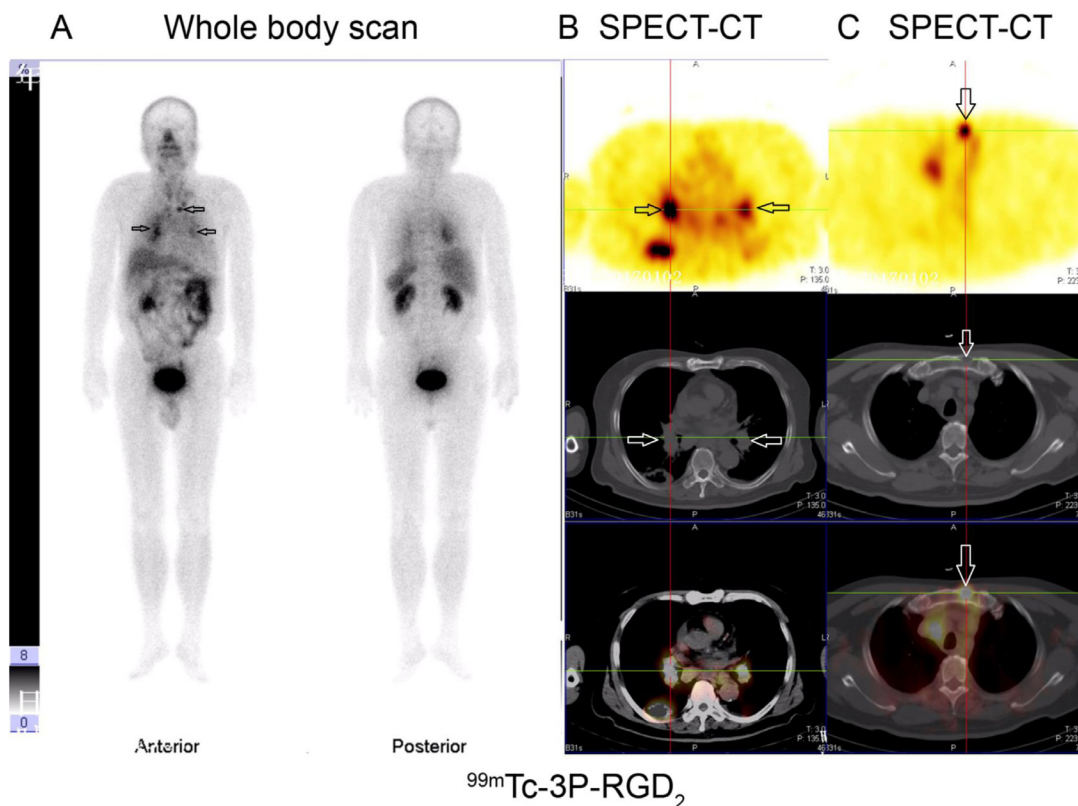


**Figure 5:**  $^{99m}\text{Tc}$ -3P-RGD<sub>2</sub> imaging of one patient with lung cancer and multi-lymph node metastases (mediastinal lymph node, hilar lymph node and presteral osteolytic). A.  $^{99m}\text{Tc}$ -3P-RGD<sub>2</sub> whole body scan; B. and C.  $^{99m}\text{Tc}$ -3P-RGD<sub>2</sub> SPECT-CT. (see arrows).

to-intense  $^{99m}\text{Tc}$ -3P-RGD<sub>2</sub> accumulation in visceral organs might make the mild-uptake lesions undetectable in lower thoracic, upper lumbar vertebra and sacrococcyx [27]. The diagnostic sensitivity of  $^{99m}\text{Tc}$ -3P-RGD<sub>2</sub> imaging for osteolytic bone metastases was significantly higher than that of  $^{99m}\text{Tc}$ -MDP imaging in our study. Also, its sensitivity was slightly lower than  $^{18}\text{F}$ -Alfatide II PET-CT imaging [18]. This may be related to the higher spatial resolution of PET and the large database. Besides detection of osteolytic bone metastases,  $^{99m}\text{Tc}$ -3P-RGD<sub>2</sub> imaging was also useful for the differential diagnosis of primary tumor and even its staging [14, 28]. In our study, primary lung cancer, thyroid cancer, malignant chromaffin-cell tumor and gastric cancer were highly positive on  $^{99m}\text{Tc}$ -3P-RGD<sub>2</sub> imaging [29]. Thus,  $^{99m}\text{Tc}$ -3P-RGD<sub>2</sub> imaging was superior to  $^{99m}\text{Tc}$ -MDP in the detection of osteolytic bone metastases, unknown primary tumor, distant metastases and clinical staging. T/N of  $^{99m}\text{Tc}$ -3P-RGD<sub>2</sub> in osteolytic metastasis may be partially influenced by integrin  $\alpha\beta$ 3 expression level on primary tumor cells [30]. In future, further studies involving more cases of different malignant tumors are needed.

In metastatic bone tissues,  $^{99m}\text{Tc}$ -MDP imaging reflects bone metabolism and osteogenesis, while  $^{99m}\text{Tc}$ -3P-RGD<sub>2</sub> imaging reflects the existence of integrin  $\alpha\beta$ 3-overexpressing tumor cells, osteoclast, angiogenesis [23, 31]. Osteolytic bone metastases usually demonstrated as increased accumulation of  $^{99m}\text{Tc}$ -3P-RGD<sub>2</sub> imaging and low uptake of  $^{99m}\text{Tc}$ -MDP. However, “hot area” or “cold area” can be visualized on both imaging modalities at the same lesion in this study. The process of osteolytic bone metastases formation is triggered by the interaction among tumor cells, bone marrow environment and bone cells (vicious cycle) [32]. The tissue component changes during the “vicious cycle” until bone destruction and structure absence. “Hot area” on both imaging modalities is possibly due to increased activation of osteolysis and osteogenesis at early stage, while “cold area” is possibly associated with bone structure resorption, destruction, internal necrosis at late stage of osteolytic bone metastasis. The CT information on SPECT-CT is important to distinguish malignant osteolytic bone destruction from benign ones when they demonstrate as “cold area” on both  $^{99m}\text{Tc}$ -3P-RGD<sub>2</sub> and  $^{99m}\text{Tc}$ -MDP imaging. Thus, these two imaging modalities are potential to play complementary roles in reflecting pathophysiological status of osteolytic lesions. In future, further studies are needed to develop targeted therapies for the management of osteolytic metastasis using  $^{177}\text{Lu}$  and  $^{90}\text{Y}$  labeled RGD peptide.

## CONCLUSIONS

Using integrin  $\alpha\beta$ 3 highly expressed in the main component of osteolytic bone metastases (e.g. tumor cells and osteoclasts) as a target,  $^{99m}\text{Tc}$ -3P-RGD<sub>2</sub> imaging demonstrated mainly as “hot region” on whole body

imaging with low background.

$^{99m}\text{Tc}$ -3P-RGD<sub>2</sub> imaging showed significantly higher detective rate than  $^{99m}\text{Tc}$ -MDP imaging based on visual and semiquantitative analysis. Such technique is potentially applicable for the detection of some unknown primary tumors and distant metastases.

## ACKNOWLEDGMENTS

We are grateful to Prof. Shuang Liu for his help in RGD dimer kit donation and Wei Gu, Muhong Guo for clinical data collection and follow-up.

This study was financially supported by grants from National Natural Science Foundation of China projects (81301247), the Natural Science Foundation of Jiangsu Province (BK20130082), Jiangsu Provincial Medical Youth Talent (QNRC2016075) and the Nanjing Outstanding Youth Fund (JQX14009).

## CONFLICTS OF INTEREST

There is no conflict of interest.

## REFERENCES

1. Ell B, Kang Y. SnapShot: Bone Metastasis. *Cell*. 2012; 151:690-690 e691. doi: 10.1016/j.cell.2012.10.005.
2. Siegel R, Ma J, Zou Z, Jemal A. Cancer statistics, 2014. *CA Cancer J Clin*. 2014; 64:9-29. doi: 10.3322/caac.21208.
3. Kakonen SM, Mundy GR. Mechanisms of osteolytic bone metastases in breast carcinoma. *Cancer*. 2003; 97:834-839. doi: 10.1002/cncr.11132.
4. Kuchuk M, Kuchuk I, Sabri E, Hutton B, Clemons M, Wheatley-Price P. The incidence and clinical impact of bone metastases in non-small cell lung cancer. *Lung Cancer*. 2015; 89:197-202. doi: 10.1016/j.lungcan.2015.04.007.
5. Braun S, Vogl FD, Naume B, Janni W, Osborne MP, Coombes RC, Schlimok G, Diel IJ, Gerber B, Gebauer G, Pierga JY, Marth C, Oruzio D, et al. A pooled analysis of bone marrow micrometastasis in breast cancer. *N Engl J Med*. 2005; 353:793-802. doi: 10.1056/NEJMoa050434.
6. Eustace S, Tello R, DeCarvalho V, Carey J, Wroblecka JT, Melhem ER Yucel EK. A comparison of whole-body turboSTIR MR imaging and planar  $^{99m}\text{Tc}$ -methylene diphosphonate scintigraphy in the examination of patients with suspected skeletal metastases. *AJR Am J Roentgenol*. 1997; 169:1655-1661. doi: 10.2214/AJR.11.8351.
7. Mouchess ML, Sohara Y, Nelson MD Jr, DeCLerck YA, Moats RA. Multimodal imaging analysis of tumor progression and bone resorption in a murine cancer model. *J Comput Assist Tomogr*. 2006; 30:525-534. doi: 10.1097/00004728-200605000-00030.
8. Peterson JJ, Kransdorf MJ, O'Connor MI. Diagnosis of occult bone metastases: positron emission tomography. *Clin*



- Orthop Relat Res. 2003; 415:S120-128. doi: 10.1097/01.blo.0000093051.96273.7c.
9. Roodman GD. Mechanisms of bone lesions in multiple myeloma and lymphoma. *Cancer*. 1997; 80:1557-1563.
  10. Mundy GR. Metastasis to bone: causes, consequences and therapeutic opportunities. *Nat Rev Cancer*. 2002; 2:584-593. doi: 10.1038/nrc867.
  11. Boissy P, Machuca I, Pfaff M, Ficheux D, Jurdic P. Aggregation of mononucleated precursors triggers cell surface expression of alphavbeta3 integrin, essential to formation of osteoclast-like multinucleated cells. *J Cell Sci*. 1998; 111:2563-2574.
  12. Chen B, Zhao G, Ma Q, Ji B, Ji T, Xin H, Gao S. (99m)Tc-3P-RGD2 SPECT to monitor early response to bevacizumab therapy in patients with advanced non-small cell lung cancer. *Int J Clin Exp Pathol*. 2015; 8:16064-16072.
  13. Jin X, Liang N, Wang M, Meng Y, Jia B, Shi X, Li S, Luo J, Luo Y, Cui Q, Zheng K, Liu Z, Shi J, et al. Integrin Imaging with 99mTc-3PRGD2 SPECT/CT Shows High Specificity in the Diagnosis of Lymph Node Metastasis from Non-Small Cell Lung Cancer. *Radiology*. 2016; 281:958-966. doi: 10.1148/radiol.2016150813.
  14. Ma Q, Ji B, Jia B, Gao S, Ji T, Wang X, Han Z, Zhao G. Differential diagnosis of solitary pulmonary nodules using (9)(9m)Tc-3P(4)-RGD(2) scintigraphy. *Eur J Nucl Med Mol Imaging*. 2011; 38:2145-2152. doi: 10.1007/s00259-011-1901-2.
  15. Zhu Z, Miao W, Li Q, Dai H, Ma Q, Wang F, Yang A, Jia B, Jing X, Liu S, Shi J, Liu Z, Zhao Z, et al. 99mTc-3PRGD2 for integrin receptor imaging of lung cancer: a multicenter study. *J Nucl Med*. 2012; 53:716-722. doi: 10.2967/jnumed.111.098988.
  16. Jia B, Liu Z, Zhu Z, Shi J, Jin X, Zhao H, Li F, Liu S, Wang F. Blood clearance kinetics, biodistribution, and radiation dosimetry of a kit-formulated integrin alphavbeta3-selective radiotracer 99mTc-3PRGD 2 in non-human primates. *Mol Imaging Biol*. 2011; 13:730-736. doi: 10.1007/s11307-010-0385-y.
  17. Shao G, Zhou Y, Wang F, Liu S. Monitoring glioma growth and tumor necrosis with the U-SPECT-II/CT scanner by targeting integrin alphavbeta3. *Mol Imaging*. 2013; 12:39-48.
  18. Mi B, Yu C, Pan D, Yang M, Wan W, Niu G, Chen X. Pilot Prospective Evaluation of (18)F-Alfatide II for Detection of Skeletal Metastases. *Theranostics*. 2015; 5:1115-1121. doi: 10.7150/thno.12938.
  19. Even-Sapir E, Metser U, Mishani E, Lievshitz G, Lerman H, Leibovitch I. The detection of bone metastases in patients with high-risk prostate cancer: 99mTc-MDP Planar bone scintigraphy, single- and multi-field-of-view SPECT, 18F-fluoride PET, and 18F-fluoride PET/CT. *J Nucl Med*. 2006; 47:287-297.
  20. Hahn S, Heusner T, Kummel S, Koninger A, Nagarajah J, Muller S, Boy C, Forsting M, Bockisch A, Antoch G, Stahl A. Comparison of FDG-PET/CT and bone scintigraphy for detection of bone metastases in breast cancer. *Acta Radiol*. 2011; 52:1009-1014. doi: 10.1258/ar.2011.100507.
  21. Kim MR, Roh JL, Kim JS, Choi SH, Nam SY, Kim SY. 18F-fluorodeoxyglucose-positron emission tomography and bone scintigraphy for detecting bone metastases in patients with malignancies of the upper aerodigestive tract. *Oral Oncol*. 2008; 44:148-152. doi: 10.1016/j.oraloncology.2007.01.011.
  22. Uchida K, Nakajima H, Miyazaki T, Tsuchida T, Hirai T, Sugita D, Watanabe S, Takeura N, Yoshida A, Okazawa H, Baba H. (18)F-FDG PET/CT for Diagnosis of Osteosclerotic and Osteolytic Vertebral Metastatic Lesions: Comparison with Bone Scintigraphy. *Asian Spine J*. 2013; 7:96-103. doi: 10.4184/asj.2013.7.2.96.
  23. Sprague JE, Kitaura H, Zou W, Ye Y, Achilefu S, Weilbaecher KN, Teitelbaum SL, Anderson CJ. Noninvasive imaging of osteoclasts in parathyroid hormone-induced osteolysis using a 64Cu-labeled RGD peptide. *J Nucl Med*. 2007; 48:311-318.
  24. Ito S, Kato K, Ikeda M, Iwano S, Makino N, Tadokoro M, Abe S, Nakano S, Nishino M, Ishigaki T, Naganawa S. Comparison of 18F-FDG PET and bone scintigraphy in detection of bone metastases of thyroid cancer. *J Nucl Med*. 2007; 48:889-895. doi: 10.2967/jnumed.106.039479.
  25. McLoughlin LC, O'Kelly F, O'Brien C, Sheikh M, Feeney J, Torreggiani W, Thornhill JA. The improved accuracy of planar bone scintigraphy by adding single photon emission computed tomography (SPECT-CT) to detect skeletal metastases from prostate cancer. *Ir J Med Sci*. 2016; 185:101-105. doi: 10.1007/s11845-014-1228-7.
  26. Zhang Y, Shi H, Gu Y, Xiu Y, Li B, Zhu W, Chen S, Yu H. Differential diagnostic value of single-photon emission computed tomography/spiral computed tomography with Tc-99m-methylene diphosphonate in patients with spinal lesions. *Nucl Med Commun*. 2011; 32:1194-1200. doi: 10.1097/MNM.0b013e32834bd82e.
  27. Miao W, Zheng S, Dai H, Wang F, Jin X, Zhu Z, Jia B. Comparison of 99mTc-3PRGD2 integrin receptor imaging with 99mTc-MDP bone scan in diagnosis of bone metastasis in patients with lung cancer: a multicenter study. *PLoS One*. 2014; 9:e111221. doi: 10.1371/journal.pone.0111221.
  28. Beer AJ, Lorenzen S, Metz S, Herrmann K, Watzlowik P, Wester HJ, Peschel C, Lordick F, Schwaiger M. Comparison of integrin alphaVbeta3 expression and glucose metabolism in primary and metastatic lesions in cancer patients: a PET study using 18F-galacto-RGD and 18F-FDG. *J Nucl Med*. 2008; 49:22-29. doi: 10.2967/jnumed.107.045864.
  29. Zhao D, Jin X, Li F, Liang J, Lin Y. Integrin alphavbeta3 imaging of radioactive iodine-refractory thyroid cancer using 99mTc-3PRGD2. *J Nucl Med*. 2012; 53:1872-1877. doi: 10.2967/jnumed.112.107821.
  30. Cheng W, Wu Z, Liang S, Fu H, Wu S, Tang Y, Ye Z,

- Wang H. Comparison of 18F-AIF-NOTA-PRGD2 and 18F-FDG uptake in lymph node metastasis of differentiated thyroid cancer. *PLoS One*. 2014; 9:e100521. doi: 10.1371/journal.pone.0100521.
31. Sutherland M, Gordon A, Shnyder SD, Patterson LH, Sheldrake HM. RGD-Binding Integrins in Prostate Cancer: Expression Patterns and Therapeutic Prospects against Bone Metastasis. *Cancers (Basel)*. 2012; 4:1106-1145. doi: 10.3390/cancers4041106.
32. Chirgwin JM, Guise TA. Molecular mechanisms of tumor-bone interactions in osteolytic metastases. *Crit Rev Eukaryot Gene Expr*. 2000; 10:159-178.